Constrained Long-Horizon Direct Model Predictive Control for Grid-Connected Converters with LCL Filters

Mattia Rossi*, Petros Karamanakos*, Francesco Castelli-Dezza†
*Tampere University, Faculty of Information Technology and Communication Sciences
33101 Tampere, Finland
†Politecnico di Milano, Department of Mechanical Engineering
20156 Milan, Italy
Email: mattia.rossi@tuni.fi, p.karamanakos@ieee.org, francesco.castellidezza@polimi.it

Keywords

≪Model predictive control≫, ≪Grid-connected converter≫, ≪Optimal control≫, ≪Multi-objective optimization≫, ≪Control methods for electrical systems≫, ≪LCL≫, ≪Converter control≫.

Abstract

This paper presents a direct model predictive control algorithm for a three-level neutral point clamped converter connected to the grid via an LCL filter. The proposed controller simultaneously controls the grid and converter currents as well as the filter capacitor voltage, while meeting the relevant grid standards. Moreover, output constraints are included to ensure operation of the system within its safe operating limits. This is achieved by formulating the direct MPC problem as a constrained integer least-squares optimization problem, wherein the output constraints are mapped into input constraints. The presented results verify the effectiveness of the proposed method.

Introduction

Medium-voltage (MV) grid-tied converters are used for the integration of renewable energy sources, scalable loads, and high-performance variable speed drives into the electrical grid. To ensure smooth operation, grid standards—e.g., the IEEE 519 [1] and the IEC 61000-2-4 [2] standards—are imposed to the point of common coupling (PCC). Such standards set tight limits on the current and voltage harmonics injected by the power electronic systems into the grid. To mitigate the current harmonics, LCL filters are commonly placed between the converter and the PCC. The addition of such a filter, however, gives rise to a third-order system, implying that its control is a nontrivial task. More specifically, not only the grid current needs to be controlled—as is the case with all grid-tied systems—but also the converter current and the capacitor voltage. Moreover, adequate damping of the filter resonance is required. Finally, large overshoots during transients that may harm the hardware components due to the correlated dynamics of the system need to be avoided to ensure safe system operation.

Meeting the above-mentioned tasks with conventional control techniques—that rely on linear control principles—is challenging, while the controller design can become complicated [3]. Furthermore, the most favorable dynamic operation is not achieved due to the cascaded control loops that tend to limit the bandwidth of the controller, especially when operation at low switching frequency is required [4]. As an alternative to linear control techniques, model predictive control (MPC) can be employed. Thanks to its multiple-input multiple-output (MIMO) nature as well as its ability to handle explicit constraints and provide active damping, superior steady-state and dynamic performance of the grid-connected power electronic system can be achieved [5, 6].

The most popular MPC-based method in academia is direct MPC, i.e., a control strategy that directly computes and applies the switching signals. Direct MPC with output reference tracking, also referred to as finite control set MPC (FCS-MPC), fully exploits the advantages that MPC can offer, but, alas, it comes with pronounced computational load [5, 7]. To address this—at least to some extent—the direct

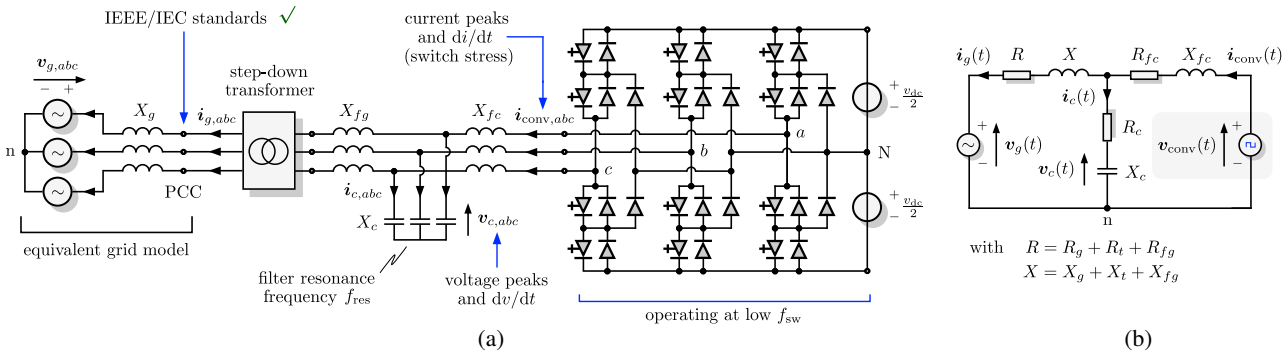

(a) (b)

Fig. 1: (a) MV grid-tied three-phase 3L-NPC converter with an *LCL*-filter placed between the converter and the step-down transformer. (b) Equivalent circuit in the $\alpha\beta$-plane.

MPC problem can be designed as an integer least-squares (ILS) one and solved with a sphere decoding algorithm [8]. Such an approach, however, cannot easily handle constraints that will ensure operation of the system within its safe operating area. Thus, to avoid overcurrents and/or overvoltages that may damage the hardware of the converter and/or the filter, the feasible set of the optimization problem underlying direct MPC needs to be carefully redesigned [9].

Given the above, this paper proposes a constrained direct MPC for an MV three-level neutral point clamped (3L-NPC) converter connected to the grid via an LCL filter. The optimization problem, formulated as an ILS one, accounts for constraints on all the controlled variables to increase the system reliability. To this aim, the output constraints are mapped into constraints on the control input. In doing so, candidate solutions that may lead to large overshoots are already excluded in a preprocessing stage. Moreover, a long horizon is employed, which combined with full-state information, provides damping of the filter resonance without requiring a dedicated active damping loop. As a result, the MV converter can be operated at a very low switching frequency (and close to the resonance), while still meeting the grid standards. The effectiveness of the adopted method is demonstrated with the presented results.

Formulation of the Constrained Direct MPC Optimization Problem

Consider the MV grid-tied 3LNPC converter with an LCL-filter shown in Fig. 1(a). To keep the demonstration of the proposed control method simple, the dc-link voltage V_{dc} is assumed to be constant[1] and the neutral point potential N fixed. All variables given in the abc-plane $\boldsymbol{\xi}_{abc} = [\xi_a\, \xi_b\, \xi_c]^T$ are mapped into two-dimensional vectors $\boldsymbol{\xi}_{\alpha\beta} = [\xi_\alpha\, \xi_\beta]^T$ via the reduced Clarke transformation matrix $\boldsymbol{K}$, i.e., $\boldsymbol{\xi}_{\alpha\beta} = \boldsymbol{K}\boldsymbol{\xi}_{abc}$, see [5].

Controller Model

The equivalent circuit of the system under consideration in the $\alpha\beta$-reference frame[2] is shown in Fig. 1(b). This paper considers the same MV conversion system as the case study described in [10], from which the system parameters are taken (see Table I in [10]). A strong grid is assumed, and the (dominant) LCL-filter resonance frequency is $f_{\text{res}} = 304\,\text{Hz}$. The passive components have very small (series) resistive parts, i.e., they essentially do not provide any passive damping. All SI variables are normalized based on the rated values of the step-down transformer (secondary side).

Depending on the *single-phase* switch position $u_z \in \mathcal{U} = \{-1, 0, 1\}$, with $z \in \{a, b, c\}$, the single-phase output voltage of a 3L-NPC converter can assume three possible discrete voltage levels, i.e., $-\frac{V_{\text{dc}}}{2}$, 0, $\frac{V_{\text{dc}}}{2}$, respectively. By introducing the *three-phase* switch position[3] $\boldsymbol{u}_{abc} = [u_a\, u_b\, u_c]^T \in \boldsymbol{\mathcal{U}} = \mathcal{U}^3$, the converter output voltage $\boldsymbol{v}_{\text{conv}}$ is given by

$$\boldsymbol{v}_{\text{conv}}(t) = \frac{V_{\text{dc}}}{2}\boldsymbol{K}\boldsymbol{u}_{abc}(t) = \frac{V_{\text{dc}}}{2}\boldsymbol{u}(t)\,. \tag{1}$$

[1]The outer layer which regulates the dc-link voltage and generates the power references is out of the scope of this paper.

[2]Hereafter, to simplify the notation, variables in the $\alpha\beta$-frame are not indicated by the corresponding subscript, unless otherwise stated.

[3]Note that, given a 3L-NPC topology, the integer input set $\boldsymbol{\mathcal{U}}$ comprises $3^3 = 27$ combinations of $\boldsymbol{u}_{abc}$

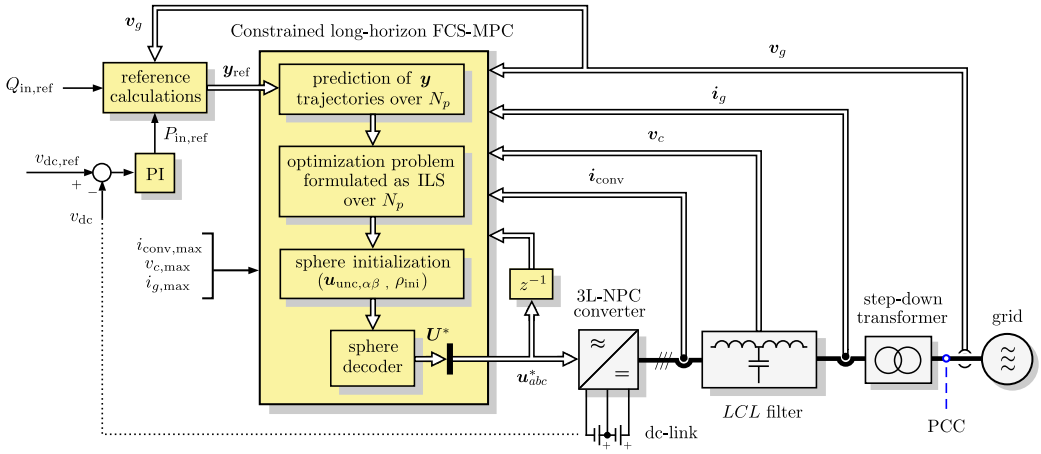

Fig. 2: Structure of the direct MPC (formulated as an ILS problem) to control the system shown in Fig. 1. The preprocessing procedure to compute ρ_{ini} is executed before calling the sphere decoder, which computes then $\boldsymbol{u}^*_{abc}$.

By choosing $\boldsymbol{x} = [\boldsymbol{i}^T_{\mathrm{conv}}\, \boldsymbol{v}^T_c\, \boldsymbol{i}^T_g\, \boldsymbol{v}^T_g]^T \in \mathbb{R}^8$ and $\boldsymbol{y} = [\boldsymbol{i}^T_{\mathrm{conv}}\, \boldsymbol{v}^T_c\, \boldsymbol{i}^T_g]^T \in \mathbb{R}^6$ as the state and output vectors, respectively, and $\boldsymbol{u} \equiv \boldsymbol{u}_{abc}$ as the control input, the continuous-time state-space representation of the system in Fig. 1(a) is

$$\frac{\mathrm{d}\boldsymbol{x}(t)}{\mathrm{dt}} = \boldsymbol{F}\boldsymbol{x}(t) + \boldsymbol{G}\boldsymbol{u}(t) \tag{2a}$$

$$\boldsymbol{y}(t) = \boldsymbol{C}\boldsymbol{x}(t)\,, \tag{2b}$$

where the voltage $\boldsymbol{v}_g$ models the grid source, $\boldsymbol{i}_g$ is the grid current, $\boldsymbol{i}_{\mathrm{conv}}$ is the converter current, while $\boldsymbol{v}_c$ is the capacitor voltage. The reader is referred to [10] for the full derivation of the continuous-time differential equations which describe the system dynamics depicted in Fig. 1(b) as well as the definition of the matrices $\boldsymbol{F} \in \mathbb{R}^{8\times 8}$, $\boldsymbol{G} \in \mathbb{R}^{8\times 3}$, and $\boldsymbol{C} \in \mathbb{R}^{6\times 8}$, respectively. Note that since an ideal grid is assumed (i.e., its angular frequency ω_g is constant), $\boldsymbol{F}$ is a time-invariant matrix. Likewise, due to the assumption of a constant dc-link voltage, $\boldsymbol{G}$ is also time invariant.

The discretized version of the continous-time system (2) is derived by using exact discretization with the sampling interval T_s, i.e.,

$$\boldsymbol{x}(k+1) = \boldsymbol{A}\boldsymbol{x}(k) + \boldsymbol{B}\boldsymbol{u}(k) \tag{3a}$$

$$\boldsymbol{y}(k) = \boldsymbol{C}\boldsymbol{x}(k)\,, \tag{3b}$$

with $\boldsymbol{A} = \mathrm{e}^{\boldsymbol{F}T_s}$ and $\boldsymbol{B} = \int_0^{T_s} e^{\boldsymbol{F}\tau}\,\mathrm{d}\tau\,\boldsymbol{G} = -\boldsymbol{F}^{-1}\,(\boldsymbol{I}_8 - \boldsymbol{A})\,\boldsymbol{G}$, while e is the matrix exponential, and $k \in \mathbb{N}$ denotes the discrete time step. Due to the absence of a modulator, T_s directly affects the switching frequency (and the *granularity of switching*), see [11].

Reformulation of the Constrained Direct MPC Problem in the Equivalent ILS Form

The block diagram of the presented MPC strategy is shown in Fig. 2. As a grid-connected power converter is considered in this work, the total demand distortion (TDD) of $\boldsymbol{i}_{g,abc}$ and $\boldsymbol{v}_{\mathrm{pcc},abc}$ as well as the amplitude of the associated harmonics should meet the IEEE 519 [1] and IEC 61000-2-4 [2] grid standards. Given this, the main control objective is to regulate $\boldsymbol{i}_g$, $\boldsymbol{i}_{\mathrm{conv}}$, and $\boldsymbol{v}_c$ along their sinusoidal references by directly manipulating the converter switches, i.e., without the use of a modulator. This needs to be achieved while operating the MV converter at a low switching frequency so that the switching power losses are kept low. The output references $\boldsymbol{y}_{\mathrm{ref}}$, i.e. $\boldsymbol{y}_{\mathrm{ref}} = [\boldsymbol{i}^T_{\mathrm{conv,ref}}\, \boldsymbol{v}^T_{c,\mathrm{ref}}\, \boldsymbol{i}^T_{g,\mathrm{ref}}]^T$, are computed based on the real $P_{\mathrm{in,ref}}$ and reactive $Q_{\mathrm{in,ref}}$ power requirements at the transformer secondary side, with $Q_{\mathrm{in,ref}} = 0$ at steady-state operation to achieve unity power factor $\mathrm{pf} = 1$. Given a prediction horizon of N_p time steps, these control objectives are mapped into a scalar by the quadratic objective function

$$J(k) = \sum_{\ell=k}^{k+N_p-1} \|\boldsymbol{y}_{\mathrm{ref}}(\ell+1) - \boldsymbol{y}(\ell+1)\|^2_{\boldsymbol{Q}} + \lambda_u\, \|\Delta\boldsymbol{u}(\ell)\|^2_2\,. \tag{4}$$

The first term in (4) denotes the deviation of the output variables $\boldsymbol{y}$ from their reference values $\boldsymbol{y}_{\mathrm{ref}}$. This error is weighted with the 6×6 positive semidefinite matrix $\boldsymbol{Q} \succeq \boldsymbol{0}$, the diagonal entries of which prioritize the tracking accuracy among the different controlled variables. The second term in (4) penalizes the switching effort, i.e., $\Delta \boldsymbol{u}(\ell) = \boldsymbol{u}(\ell) - \boldsymbol{u}(\ell-1)$, which directly relates to the definition of the average device switching frequency f_{sw} [11]. To set the trade-off between the tracking accuracy and the resulting f_{sw} at each time step $\ell = k, \ldots, k+N_p-1$, the weighting factor $\lambda_u \in \mathbb{R}^{++}$ is introduced.

The aforementioned control goals have to be met while protecting the switching devices and LCL filter components from overcurrents and overvoltages, respectively. Therefore, during power transients, the amplitudes of $\boldsymbol{i}_{\mathrm{conv}}$, $\boldsymbol{v}_c$, and $\boldsymbol{i}_g$ must be kept within given bounds. To this end, soft constraints are typically introduced in the optimization problem to include such physical limitations. Nevertheless, hard constraints are implemented in this work to facilitate the reformulation of the optimization problem, as shown in later sections. Hence, the constraints on the system output are designed in the $\alpha\beta$-plane and imposed at each time step $\ell+1$, i.e.,

$$\|\boldsymbol{i}_{\mathrm{conv}}(\ell+1)\|_2 \leq i_{\mathrm{conv,max}}\,, \qquad \|\boldsymbol{v}_c(\ell+1)\|_2 \leq v_{c,\mathrm{max}}\,, \qquad \|\boldsymbol{i}_g(\ell+1)\|_2 \leq i_{g,\mathrm{max}}\,, \tag{5}$$

where the positive scalars $i_{\mathrm{conv,max}}$, $v_{c,\mathrm{max}}$, $i_{g,\mathrm{max}} \in \mathbb{R}^{+}$ define the upper boundary values of the converter current, filter capacitor voltage, and grid current, respectively. As an example, considering $\boldsymbol{i}_{\mathrm{conv}}$ bounded by $i_{\mathrm{conv,max}}$, it follows that

$$i^2_{\mathrm{conv},\alpha}(\ell+1) + i^2_{\mathrm{conv},\beta}(\ell+1) \leq i^2_{\mathrm{conv,max}}\,, \tag{6}$$

which defines a circle in the $\alpha\beta$-plane of radius $i_{\mathrm{conv,max}}$. The constraints on $\boldsymbol{v}_c$ and $\boldsymbol{i}_g$ are imposed in a similar manner by referring to $v_{c,\mathrm{max}}$ and $i_{g,\mathrm{max}}$, respectively.

Given the above, to compute the optimal switching sequence over the N_p prediction steps[4], i.e., $\boldsymbol{U}^*(k) = \left[\boldsymbol{u}^{*T}(k)\, \boldsymbol{u}^{*T}(k+1)\, \ldots\, \boldsymbol{u}^{*T}(k+N_p-1)\right]^T \in \mathbb{U} = \boldsymbol{\mathcal{U}} \times \ldots \times \boldsymbol{\mathcal{U}} = \boldsymbol{\mathcal{U}}^{N_p} \subset \mathbb{Z}^{3N_p}$, that results in the best system performance—as quantified by (4)—while respecting the system dynamics and constraints—as expressed by (3) and (5), respectively—the constrained optimization problem underlying MPC needs to be solved. As shown in [8], to mitigate the computational burden of long-horizon direct MPC, while still guaranteeing optimality, function (4) can be written such that the associated optimization problem is a truncated ILS one. This problem can be subsequently solved in a computationally efficient manner with a dedicated branch-and-bound strategy named *sphere decoder* [8], [12].

By considering the unconstrained solution $\boldsymbol{U}_{\mathrm{unc}}$, i.e., the solution that minimizes (4) when relaxing the feasible set from $\mathbb{U}$ to $\mathbb{R}^{3N_p}$, the following equivalent constrained ILS problem can be defined

$$\boldsymbol{U}^*(k) = \arg \underset{\boldsymbol{U}(k) \in \mathbb{U}}{\text{minimize}} \;\; \left\|\boldsymbol{V}\boldsymbol{U}(k) - \bar{\boldsymbol{U}}_{\mathrm{unc}}(k)\right\|_2^2 \tag{7a}$$

$$\text{subject to} \;\; \boldsymbol{U}(k) \in \mathbb{U} = \boldsymbol{\mathcal{U}}^{N_p}\,, \quad \|\Delta \boldsymbol{u}(\ell)\|_\infty \leq 1\,, \tag{7b}$$

$$\|\boldsymbol{i}_{\mathrm{conv}}(\ell+1)\|_2 \leq i_{\mathrm{conv,max}}\,, \quad \|\boldsymbol{v}_c(\ell+1)\|_2 \leq v_{c,\mathrm{max}}\,, \tag{7c}$$

$$\|\boldsymbol{i}_g(\ell+1)\|_2 \leq i_{g,\mathrm{max}}\,, \quad \forall \ell = k, \ldots, k+N_p-1\,, \tag{7d}$$

where $\bar{\boldsymbol{U}}_{\mathrm{unc}}(k) = \boldsymbol{V}\boldsymbol{U}_{\mathrm{unc}}(k) \in \mathbb{R}^{3N_p}$, and $\boldsymbol{V} \in \mathbb{R}^{3N_p \times 3N_p}$ is a nonsingular, upper triangular matrix, known as the *lattice generator* matrix. The latter generates the $3N_p$-dimensional discrete space (lattice), one point of which is the solution to problem (7), i.e., the lattice point with the shortest Euclidean distance to $\bar{\boldsymbol{U}}_{\mathrm{unc}}$. Note that, a further (hard) input constraint, i.e., $\|\Delta \boldsymbol{u}(\ell)\|_\infty \leq 1$, with $\Delta \boldsymbol{u}(\ell) = \boldsymbol{u}(\ell) - \boldsymbol{u}(\ell-1)$, is imposed by (7b) to avoid a shoot-through in the converter due to the 3L-NPC topology [5]. Out of $\boldsymbol{U}^*$, only the first element $\boldsymbol{u}^*$ is applied to the converter whereas the rest are discarded in line with the receding horizon (RH) control principle [13]. Following, the optimization procedure is repeated at $k+1$ based on a new $\boldsymbol{x}(k)$ and a shifted prediction horizon N_p.

Note that the initial radius of the sphere ρ_{ini} affects the effectiveness of the search process as it defines the first upper bound of the branch-and-bound mechanism. Therefore, ρ_{ini} should be as small as possible

[4]Note that, the *feasible set* $\mathbb{U}$ is defined by the N_p-times Cartesian product of $\boldsymbol{\mathcal{U}}$

to remove a priori as many candidate solutions as possible, while still ensuring feasibility of the optimization process, e.g., containing at least one lattice point. In [14], the initial radius ρ_{ini} is computed as

$$\rho_{\text{ini}}(k) = \min\{\, \rho_1(k), \rho_2(k) \,\}\ , \tag{8}$$

where the relative options are

$$\rho_1(k) = \left\| \bar{\boldsymbol{U}}_{\text{unc}}(k) - \boldsymbol{V}\boldsymbol{U}_{\text{bab}}(k) \right\|_2 \qquad \text{and} \qquad \rho_2(k) = \left\| \bar{\boldsymbol{U}}_{\text{unc}}(k) - \boldsymbol{V}\boldsymbol{U}_{\text{ed}}(k) \right\|_2 . \tag{9}$$

Radius ρ_1 in (9) depends on the Babai estimate $\boldsymbol{U}_{\text{bab}}$, which is the rounded unconstrained solution, i.e., $\boldsymbol{U}_{\text{bab}}(k) = \lfloor \boldsymbol{U}_{\text{unc}}(k) \rceil$. On the other hand, radius ρ_2 in (9) depends on an educated guess $\boldsymbol{U}_{\text{ed}}$, which is the previously applied solution $\boldsymbol{U}^*(k-1)$ shifted by one time step according to the RH policy, see [9].

Solving the Equivalent Constrained Integer Least-Squares Problem

The presence of constraint (7) affects the aforementioned computation of ρ_{ini}. Indeed, by adopting (8), there is a possibility that $\boldsymbol{U}_{\text{unc}}$ and/or some of the candidate solutions included in the sphere violate (7). To avoid this, the computation of the initial radius needs to be revised. This is done by mapping the output constraints (7) into (hard) input constraints, thus limiting the feasible set $\mathbb{U}$. The approach presented in this paper is based on [9] and extended to handle multiple constraints by simultaneously considering bounds on $\boldsymbol{i}_{\text{conv}}$, $\boldsymbol{v}_c$, and $\boldsymbol{i}_g$.

By utilizing (3a) and (3b), the output dynamics at step $k+1$ are given by

$$\boldsymbol{y}(k+1) = \boldsymbol{C}\boldsymbol{A}\boldsymbol{x}(k) + \boldsymbol{C}\widetilde{\boldsymbol{B}}\boldsymbol{K}\boldsymbol{u}(k) \ \Rightarrow\ \boldsymbol{i}_{\text{conv}}(k+1) = [\ \boldsymbol{I}_2\ \ \boldsymbol{0}_{2\times 6}\ ]\,\boldsymbol{A}\boldsymbol{x}(k) + \gamma_{\text{conv}}\boldsymbol{I}_2\boldsymbol{u}_{\alpha\beta}(k) \tag{10a}$$

$$\boldsymbol{v}_c(k+1) = [\ \boldsymbol{0}_{2\times 2}\ \ \boldsymbol{I}_2\ \ \boldsymbol{0}_{2\times 4}\ ]\,\boldsymbol{A}\boldsymbol{x}(k) + \gamma_c\boldsymbol{I}_2\boldsymbol{u}_{\alpha\beta}(k) \tag{10b}$$

$$\boldsymbol{i}_g(k+1) = [\ \boldsymbol{0}_{2\times 4}\ \ \boldsymbol{I}_2\ \ \boldsymbol{0}_{2\times 2}\ ]\,\boldsymbol{A}\boldsymbol{x}(k) + \gamma_g\boldsymbol{I}_2\boldsymbol{u}_{\alpha\beta}(k)\,, \tag{10c}$$

where $\widetilde{\boldsymbol{B}} = -\boldsymbol{F}^{-1}(\boldsymbol{I}_8 - \boldsymbol{A})\,\widetilde{\boldsymbol{G}}$, with $\widetilde{\boldsymbol{G}} = (V_{\text{dc}}/2X_{fc})\,[\boldsymbol{I}_2\ \boldsymbol{0}_{2\times 6}]^T$. Moreover, $\boldsymbol{u}_{\alpha\beta}(k) = \boldsymbol{K}\boldsymbol{u}(k)$, while $\boldsymbol{C}\widetilde{\boldsymbol{B}}\boldsymbol{K} = \boldsymbol{C}\boldsymbol{B}$ holds. In more detail, given $\boldsymbol{C} \in \mathbb{R}^{6\times 8}$ and $\widetilde{\boldsymbol{B}} \in \mathbb{R}^{8\times 2}$, (10a), (10b), and (10c), are derived by noticing the structure of the product $\boldsymbol{C}\widetilde{\boldsymbol{B}} \in \mathbb{R}^{6\times 2}$, i.e.,

$$\boldsymbol{C}\widetilde{\boldsymbol{B}} = \begin{bmatrix} \gamma_{\text{conv}} & 0 & \gamma_c & 0 & \gamma_g & 0 \\ 0 & \gamma_{\text{conv}} & 0 & \gamma_c & 0 & \gamma_g \end{bmatrix}^T = \begin{bmatrix}\ \gamma_{\text{conv}}\boldsymbol{I}_2 & \gamma_c\boldsymbol{I}_2 & \gamma_g\boldsymbol{I}_2\ \end{bmatrix}^T . \tag{11}$$

As can be seen in (11), three 2×2 diagonal matrices appear, i.e., $\text{diag}(\gamma_{\text{conv}}) \succ 0 \in \mathbb{R}^{2\times 2}$, $\text{diag}(\gamma_c) \succ 0 \in \mathbb{R}^{2\times 2}$, and $\text{diag}(\gamma_g) \succ 0 \in \mathbb{R}^{2\times 2}$, with $\gamma_{\text{conv}} \neq \gamma_c \neq \gamma_g$. In particular, $\gamma_{\text{conv}}\boldsymbol{I}_2 = [\boldsymbol{I}_2\ \boldsymbol{0}_{2\times 6}]\,\widetilde{\boldsymbol{B}}$, $\gamma_c\boldsymbol{I}_2 = [\boldsymbol{0}_{2\times 2}\ \ \boldsymbol{I}_2\ \ \boldsymbol{0}_{2\times 4}]\,\widetilde{\boldsymbol{B}}$ and $\gamma_g\boldsymbol{I}_2 = [\boldsymbol{0}_{2\times 4}\ \ \boldsymbol{I}_2\ \ \boldsymbol{0}_{2\times 2}]\,\widetilde{\boldsymbol{B}}$ can be easily computed. Given (10a), (10b), and (10c), the three one-dimensional constraints in (5) can be rewritten as

$$\|\boldsymbol{i}_{\text{conv}}(\ell+1)\|_2 \le i_{\text{conv,max}} \ \Rightarrow\ \left\| \frac{[\ \boldsymbol{I}_2\ \ \boldsymbol{0}_{2\times 6}\ ]\,\boldsymbol{A}\boldsymbol{x}(k)}{\gamma_{\text{conv}}} + \boldsymbol{K}\boldsymbol{u}(k) \right\|_2 \le \frac{i_{\text{conv,max}}}{\gamma_{\text{conv}}} \tag{12a}$$

$$\|\boldsymbol{v}_c(\ell+1)\|_2 \le v_{c,\text{max}} \ \Rightarrow\ \left\| \frac{[\ \boldsymbol{0}_{2\times 2}\ \ \boldsymbol{I}_2\ \ \boldsymbol{0}_{2\times 4}\ ]\,\boldsymbol{A}\boldsymbol{x}(k)}{\gamma_c} + \boldsymbol{K}\boldsymbol{u}(k) \right\|_2 \le \frac{v_{c,\text{max}}}{\gamma_c} \tag{12b}$$

$$\|\boldsymbol{i}_g(\ell+1)\|_2 \le i_{g,\text{max}} \ \Rightarrow\ \left\| \frac{[\ \boldsymbol{0}_{2\times 4}\ \ \boldsymbol{I}_2\ \ \boldsymbol{0}_{2\times 2}\ ]\,\boldsymbol{A}\boldsymbol{x}(k)}{\gamma_g} + \boldsymbol{K}\boldsymbol{u}(k) \right\|_2 \le \frac{i_{g,\text{max}}}{\gamma_g}\,. \tag{12c}$$

To simplify the derivation of the constrained ILS problem, let us first consider a generic one-dimensional constraint of the form

$$\left\| \frac{\widetilde{\boldsymbol{C}}\boldsymbol{A}\boldsymbol{x}(k)}{\gamma} + \boldsymbol{K}\boldsymbol{u}(k) \right\|_2 \le \frac{y_{\text{max}}}{\gamma} \quad \Longleftrightarrow \quad \|\boldsymbol{u}_{\text{constr}}(k) + \boldsymbol{K}\boldsymbol{u}(k)\|_2 \le \rho_{\text{constr}}\,, \tag{13}$$

where the generic $\widetilde{\boldsymbol{C}}$, γ, and y_{max} are changed according to which constraint among (12a), (12b), and (12c) is taken into consideration. Note that (13) describes a feasible set in the form of a circle $\mathcal{C}$ in the $\alpha\beta$-plane centered at $\boldsymbol{u}_{\text{constr}}(k) = -\frac{\widetilde{\boldsymbol{C}}\boldsymbol{A}\boldsymbol{x}(k)}{\gamma}$ with radius $\rho_{\text{constr}} = \frac{y_{\text{max}}}{\gamma}$.

With (13), the constraints in (12) define $\mathcal{C}_{\text{conv}}$, $\mathcal{C}_c$, and $\mathcal{C}_g$ related to $\boldsymbol{i}_{\text{conv}}$, $\boldsymbol{v}_c$, and $\boldsymbol{i}_g$, respectively,

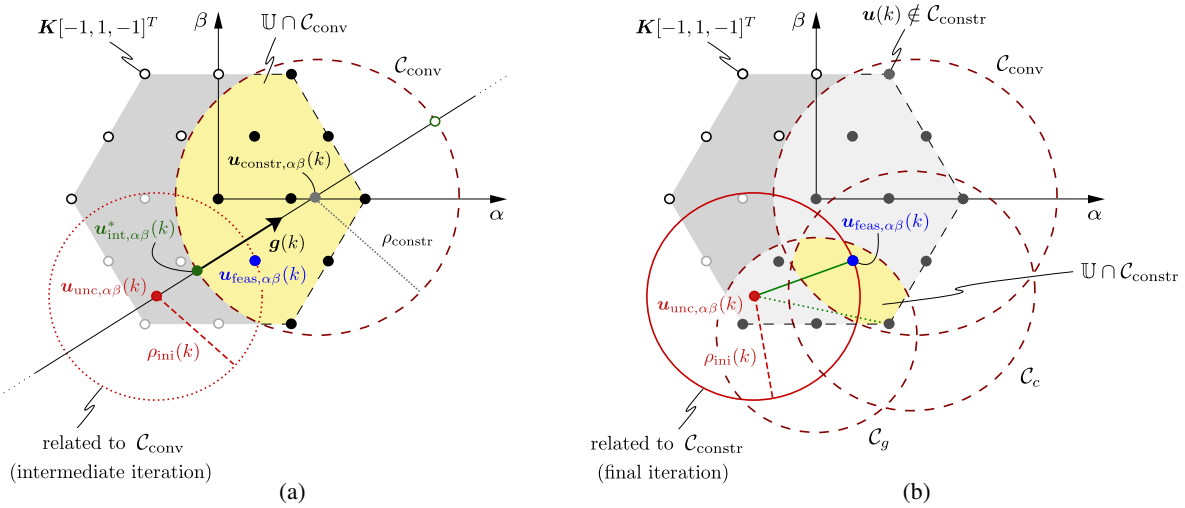

Fig. 3: Computation of the input constrained set $\mathcal{C}_{\text{constr}}$ and choice of the initial radius in the $\alpha\beta$-plane. (a) Computation of $\rho_{\text{ini}}(k)$ for a one-dimensional constraint (set $\mathcal{C}_{\text{conv}}$). (b) Computation of $\mathcal{C}_{\text{constr}}$ and $\rho_{\text{ini}}(k)$ based on all three constraints. Focusing on (a), the gradient, as depicted by the (scaled-down) vector $\boldsymbol{g}(k)$, shows the relative position of $\boldsymbol{u}_{\text{unc}}(k)$ with respect to the center of $\mathcal{C}_{\text{conv}}$, i.e., $\boldsymbol{u}_{\text{constr}}(k)$. Subsequently, the intersection point between $\boldsymbol{g}(k)$ and $\mathcal{C}_{\text{conv}}$, i.e., $\boldsymbol{u}^*_{\text{int}}(k)$ (indicated as green circle), that is closer to $\boldsymbol{u}_{\text{unc}}(k)$ (shown as red circle) is rounded up. Based on $\boldsymbol{u}_{\text{feas}}(k)$ (shown as blue circle) the radius $\rho_{\text{ini}}(k)$ (red dash-dotted line) of the hypersphere (shown as a red circle) is determined. The infeasible points enclosed in the hypersphere are indicated with light gray circles, whereas the black solid circles are feasible, but suboptimal, points.

which individually restrict the feasible set $\mathbb{U}$. This implies that to meet the output constraint (7), the optimal switching sequence $\boldsymbol{U}^*$ should lie within the intersection of all the constrained sets $\mathcal{C}_{\text{constr}} = \mathcal{C}_{\text{conv}} \cap \mathcal{C}_c \cap \mathcal{C}_g$ in the $\alpha\beta$-plane. Based on this, the *feasible* set of the integer-valued input vector $\boldsymbol{U}$ is defined as $\mathbb{U}_{\text{constr}} = \mathbb{U} \cap \mathcal{C}_{\text{constr}} = \boldsymbol{\mathcal{U}}_{\text{constr},1} \times \ldots \times \boldsymbol{\mathcal{U}}_{\text{constr},N_p}$, with

$$\boldsymbol{\mathcal{U}}_{\text{constr},i} = \{\boldsymbol{u}(\ell) \mid \boldsymbol{K}\boldsymbol{u}(\ell) \in \mathcal{C}_{\text{constr}},\ \boldsymbol{u}(\ell) \in \boldsymbol{\mathcal{U}}\} \qquad \forall \ell = k, \ldots, k+N_p-1\,, \tag{14}$$

for $i \in \{1, \ldots, N_p\}$. A graphical example is depicted in Fig. 3(a).

Given (14), the initial radius ρ_{ini} of the hypersphere needs to be revised according to the restricted input feasible set $\mathbb{U}_{\text{constr}}$. While on the one hand the radius should meet the same objective as in the unconstrained ILS problem case, i.e., to be as small as possible, an additional goal is that the new hypersphere should include at least one *feasible* point. To satisfy both criteria, (8) is substituted by

$$\rho_{\text{ini}}(k) = \min\{\,\widehat{\rho}_1(k), \widehat{\rho}_2(k)\,\}\,. \tag{15}$$

To compute ρ_{ini} in presence of the multiple output constraints, the following procedure is adopted.

Step 1: Radius $\widehat{\rho}_1$ is defined as

$$\widehat{\rho}_1(k) = \left\|\bar{\boldsymbol{U}}_{\text{unc}}(k) - \boldsymbol{V}\boldsymbol{U}_{\text{rnd}}(k)\right\|_2\,, \tag{16}$$

where the new initial guess $\boldsymbol{U}_{\text{rnd}}(k) = \left[\boldsymbol{u}^T_{\text{rnd}}(k)\ \ldots\ \boldsymbol{u}^T_{\text{rnd}}(k+N_p-1)\right]^T$ in the $\alpha\beta$-plane is equal to the Babai estimate $\boldsymbol{U}_{\text{bab}}$ from time step $k+1$ up to $k+N_p-1$, whereas the estimate at k results by guessing the feasible candidate solution $\boldsymbol{u}_{\text{feas}}(k) = \boldsymbol{K}\boldsymbol{u}_{\text{feas},abc}(k)$, with $\boldsymbol{u}_{\text{feas},abc} \in \boldsymbol{\mathcal{U}}_{\text{constr},1}$, closest to $\boldsymbol{u}_{\text{unc}}$ [9].

Step 2: Considering a single (one-dimensional) output constraint, the vector $\boldsymbol{g}(k) = \boldsymbol{u}_{\text{constr}}(k) - \boldsymbol{u}_{\text{unc}}(k)$ that spans the line passing through $\boldsymbol{u}_{\text{unc}}$ and the center of $\mathcal{C}$, i.e., $\boldsymbol{u}_{\text{constr}}$, is computed.

Step 3: The intersection points, $\boldsymbol{u}_{\text{int},1}$ and $\boldsymbol{u}_{\text{int},2}$, of the aforementioned line and $\mathcal{C}$ are calculated. The one closer to $\boldsymbol{u}_{\text{unc}}$ is computed with

$$\boldsymbol{u}^*_{\text{int}}(k) = \arg\text{minimize}\ \left\|\boldsymbol{u}_{\text{int},i}(k) - \boldsymbol{u}_{\text{unc}}(k)\right\|_2 \quad \text{for } i = 1, 2\,.$$

Step 4: The feasible input closer to $\boldsymbol{u}^*_{\rm int}$ is found. This is done by examining the sign of the elements of $\boldsymbol{g}(k)$, i.e., the direction of the gradient in each dimension of the space. Following, $\boldsymbol{u}^*_{\rm int}$ is *rounded* up or down (i.e., ceiled or floored, respectively) depending on the direction of the gradient, i.e.,

$$\boldsymbol{u}_{\rm feas}(k) = \begin{cases} \lceil \boldsymbol{u}^*_{\rm int}(k) \rceil & \text{if } \boldsymbol{g}(k) \geq 0 \\ \lfloor \boldsymbol{u}^*_{\rm int}(k) \rfloor & \text{if } \boldsymbol{g}(k) < 0\,. \end{cases} \tag{17}$$

Step 5: The candidate solution $\boldsymbol{u}_{\rm feas}$—mapped onto the three-phase switch position by $\boldsymbol{u}_{{\rm feas},abc}(k) = \boldsymbol{K}^{-1}\boldsymbol{u}_{\rm feas}(k)$—is the initial guess at time-step k. As for radius $\widehat{\rho}_2$, this depends on the educated guess $\boldsymbol{U}_{\rm ed}$. However, it is finite only if $\boldsymbol{U}_{\rm ed}$ belongs to the constrained feasible set, i.e.,

$$\widehat{\rho}_2(k) = \begin{cases} \rho_2(k) & \text{if } \boldsymbol{U}_{\rm ed}(k) \in \mathbb{U}_{\rm constr} \\ \infty & \text{if } \boldsymbol{U}_{\rm ed}(k) \notin \mathbb{U}_{\rm constr}\,. \end{cases} \tag{18}$$

Then, the initial radius is found by solving $\rho_{\rm ini}(k) = \min\{\,\widehat{\rho}_1(k), \widehat{\rho}_2(k)\,\}$.

At this point it should be mentioned that by adopting steps 1–5 for each one-dimensional constraint, three values of $\rho_{\rm ini}$—related to three different values of $\boldsymbol{u}_{\rm feas}$—result. Hence, the new hypersphere should contain at least one point/solution within $\mathcal{C}_{\rm constr} = \mathcal{C}_{\rm conv} \cap \mathcal{C}_c \cap \mathcal{C}_g$. To achieve this, the following step is introduced.

Step 6: For each one-dimensional constraint $j \in \{1, 2, 3\}$, the outcome of steps 1–5 is $\boldsymbol{u}_{{\rm feas},j}$ (see (17)) that relates to $\rho_{{\rm ini},j}$. Thus, $\boldsymbol{u}_{{\rm feas},j}$ which lies in $\mathcal{C}_{\rm constr}$ is selected and the related $\rho_{{\rm ini},j}$ is used to build the sphere. If multiple $\boldsymbol{u}_{{\rm feas},j}$ lie in $\mathcal{C}_{\rm constr}$, the one with the minimal distance from $\boldsymbol{u}_{\rm unc}$ is selected[5].

To elucidate the above-mentioned procedure, the example in Fig. 3(b) is provided. Therein, the three output constraints are visualized, with $\boldsymbol{u}_{\rm feas,1} \leftarrow \mathcal{C}_{\rm conv}$, $\boldsymbol{u}_{\rm feas,2} \leftarrow \mathcal{C}_c$, and $\boldsymbol{u}_{\rm feas,3} \leftarrow \mathcal{C}_g$, while only one candidate solution is assumed to lie in $\mathcal{C}_{\rm constr}$ at time step k to simplify the demonstration. After computing the feasible input set and the refined initial radius, the sphere decoder is called with the difference that now the $3N_p$-dimensional candidate solution $\boldsymbol{U}^*(k)$ enclosed in the hypersphere belongs to set $\mathbb{U}_{\rm constr} = \mathbb{U} \cap \mathcal{C}_{\rm constr}$. Nevertheless, in the worst-case scenario, if none of the resulting $\boldsymbol{u}_{{\rm feas},j}$ computed from steps 1–6 belongs to $\mathcal{C}_{\rm constr}$, the set is first relaxed to $\mathcal{C}_{\rm constr} = \mathcal{C}_{\rm conv} \cap \mathcal{C}_c$, and then to $\mathcal{C}_{\rm constr} = \mathcal{C}_{\rm conv}$ in order to find the that best suboptimal solution that violates the smallest number of constraints.

Performance Assessment

The performance of the proposed direct MPC scheme is evaluated through MATLAB simulations. Considering $f_{\rm res} = 304\,\text{Hz}$, the goal is to choose λ_u such that the switching frequency $f_{\rm sw}$ is close to $f_{\rm res}$. To this aim, λ_u is chosen such that $f_{\rm sw} \approx 400\,\text{Hz}$ results, i.e., $\lambda_u = 0.45$. A sampling interval $T_s = 150\,\mu\text{s}$ is chosen such that a high granularity of switching is achieved, as this improves the system performance [11]. Moreover, given that for a favorable steady-state and transient performance a long prediction interval in time is recommended [15], a ten-step ($N_p = 10$) horizon is implemented. Regarding the matrix $\boldsymbol{Q}$, the tracking of $\boldsymbol{i}_{g,abc}$ is prioritized over the reference tracking of the other variables to reduce the grid current TDD, $I_{g,\rm TDD}$. Then, the converter current tracking is prioritized with respect to the voltage capacitor to (indirectly) avoid a deterioration in the tracking performance of $\boldsymbol{i}_{g,abc}$. This yields $\boldsymbol{Q} = \text{diag}\,(10, 10, 1, 1, 100, 100)$. The upper bounds $i_{\rm conv,max} = 1.3$ per unit (p.u.), $v_{c,\rm max} = 1.25\,\text{p.u.}$, and $i_{g,\rm max} = 1.25\,\text{p.u.}$ are considered to limit overshoots during transients. Note that, given the chosen limits, the hard constraints do not affect the steady-state operation. All results in the sequel are in p.u.

Both steady-state and transient performances are depicted in Fig. 4 over two fundamental periods. More specifically, Fig. 4(a) shows the three-phase output waveforms produced by a direct MPC formulation without output bounds, i.e., when neglecting (7) and computing $\rho_{\rm ini}$ as in (8). On the other hand, Fig. 4(b) depicts the system response when the constrained MPC is taken into account, i.e., when considering (7) and the modified radius is computed according to (15).

[5]Note that, this procedure can be also adopted to evaluate a larger number of constraints n_c, i.e. $j = 1, ..., n_c$

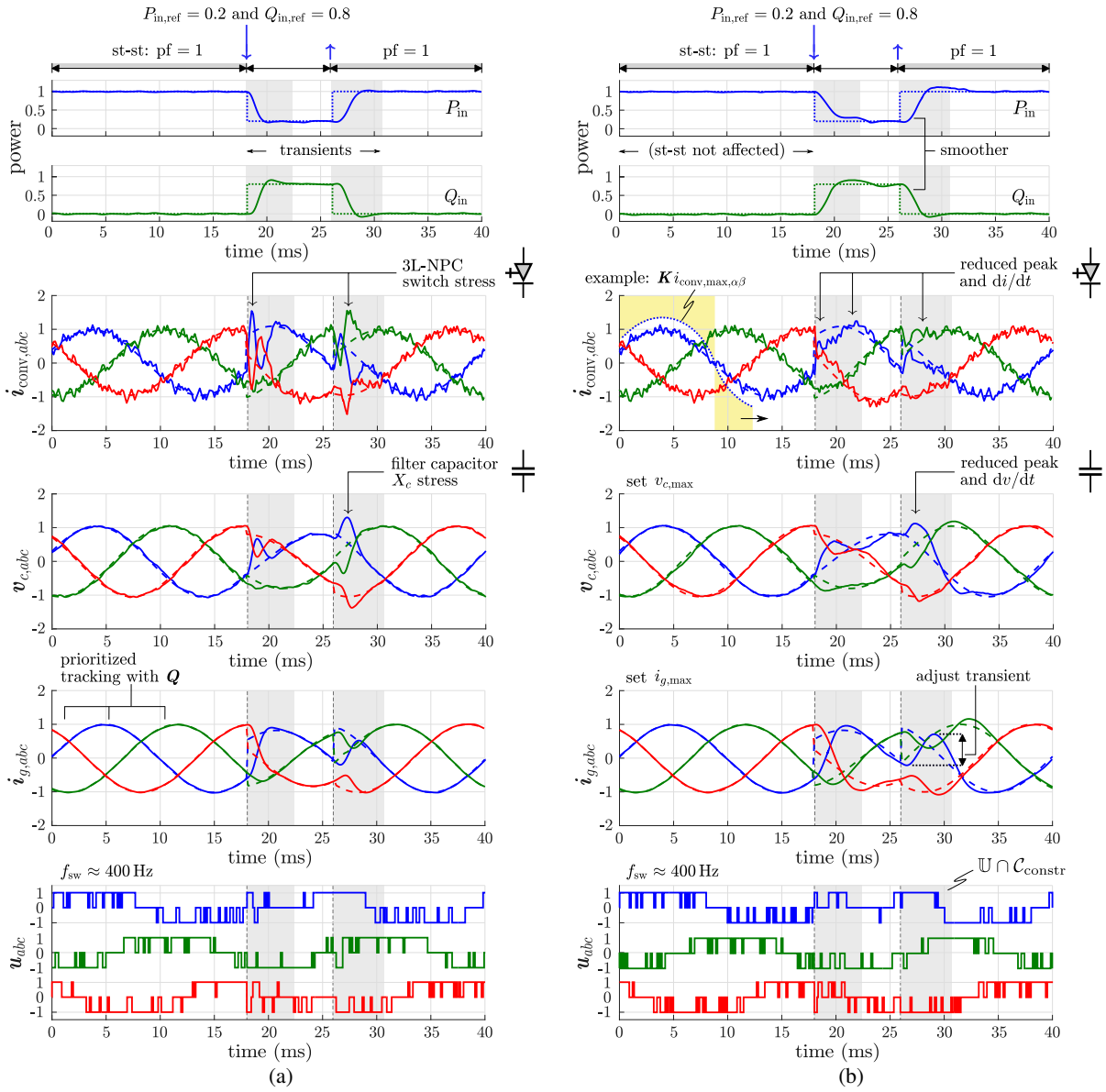

Fig. 4: Simulated waveforms produced by direct MPC when the output constraints are (a) not included, and (b) included. The results are shown over two fundamental periods $2T_g$, with $T_g = 20$ ms. From top to bottom: real P_{in} (blue line) and reactive power Q_{in} (green line) and their references (dashed lines); three-phase converter currents $\boldsymbol{i}_{\text{conv},abc}$ (with a, b and c shown with blue, red, and green lines, respectively) and the related references; three-phase capacitor voltage $\boldsymbol{v}_{c,abc}$; three-phase grid currents $\boldsymbol{i}_{g,abc}$; three-phase switch position $\boldsymbol{u}_{abc}$.

Large step-wise changes in the input power references are applied. At $t = 18$ ms, $P_{\text{in,ref}}$ is changed from 1 to 0.2 p.u. and back to 1 p.u. at $t = 26$ ms. Likewise, $Q_{\text{in,ref}}$ is changed from 0 to 0.8 p.u. and back to 0 p.u. at the same time instants. The power references are translated into the corresponding $\boldsymbol{y}_{\text{ref},abc}$ which are accurately followed by $\boldsymbol{y}_{abc}$. As shown in Fig. 4(a), when the output constraints are not considered, the variables $\boldsymbol{i}_{\text{conv},abc}$ and $\boldsymbol{v}_{c,abc}$ exhibit significant overshoots during transients, exceeding the associated trip levels defined by the translation of $i_{\text{conv,max}}$ and $v_{c,\text{max}}$ into the abc-plane via $\boldsymbol{K}$. To provide more insight into this point, and since the constraints are given in the $\alpha\beta$-plane, the dynamics in Fig. 4 are translated accordingly and shown in Fig. 5. In particular, given the time window from $t = 15$ ms to $t = 35$ ms, Fig. 5(a) shows and quantifies the violation of $\boldsymbol{y}_{abc}$. For example, as can be seen, $\boldsymbol{i}_{\text{conv},\alpha\beta}$ presents a peak of 1.70 p.u. which is 40% above $i_{\text{conv,max}} = 1.3$ p.u.

On the other hand, the effectiveness of the constrained MPC algorithm can be appreciated in Figs. 4(b) and 5(b), where $\boldsymbol{y}_{abc}$ (and $\boldsymbol{y}_{\alpha\beta}$) always remain within the imposed bounds. It is worth mentioning, however, that the constrained MPC is less aggressive since the output bounds restrict the input set to $\mathbb{U}_{\text{constr}} \subset \mathbb{U}$, i.e., the candidate solutions that could lead to faster settling times are limited as these can lead to violation of the constraints. This implies that the decisions the MPC algorithm makes when the

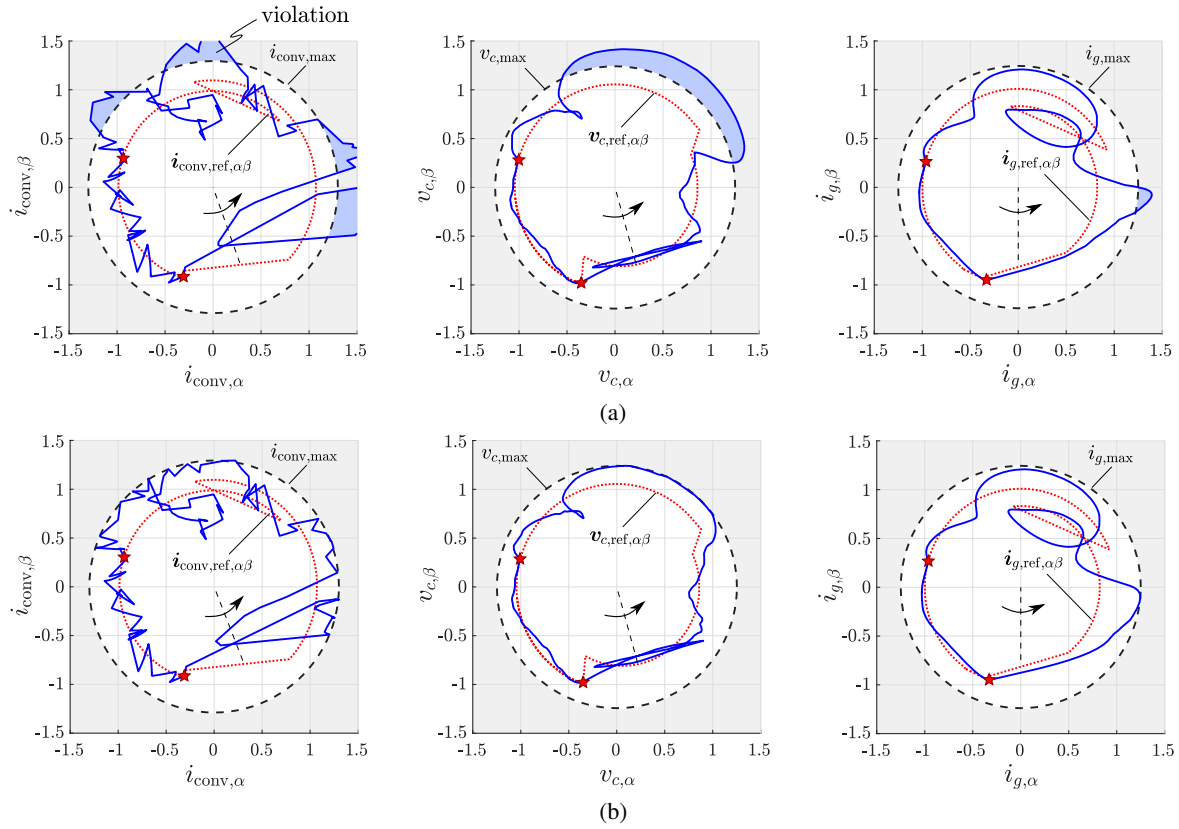

Fig. 5: Simulated waveforms of $\boldsymbol{i}_{\text{conv},\alpha\beta}$ (left), $\boldsymbol{v}_{c,\alpha\beta}$ (center), and $\boldsymbol{i}_{g,\alpha\beta}$ (right) produced by the proposed direct MPC algorithm when output constraints are (a) not included, and (b) included. The references and bounds are shown as (red) dotted and (black) dashed circles, respectively. The $\alpha\beta$-plots cover a time window from 15 to 35 ms. All variables in Fig. 4 are mapped from abc to $\alpha\beta$, i.e. $\boldsymbol{\xi}_{\alpha\beta} = \boldsymbol{K}\boldsymbol{\xi}_{abc}$.

output constraints are active would correspond to suboptimal solutions compared to the case where the constraints are not considered. As a result, the settling times of the power transients in Figs. 4(b) are slightly longer compared to Fig. 4(a).

Finally, it worth mentioning that when operating at steady-state—i.e., $P_{\text{in,ref}} = 1$ and $Q_{\text{in,ref}} = 0$ with $\text{pf} = 1$—the output constraints are not activated, hence both MPC algorithms perform the same.[6] In both cases, all output variables $\boldsymbol{y}_{abc}$ accurately track their sinusoidal reference values, despite operation at a switching frequency that is very close to the resonance one. The current and PCC voltage harmonic spectra produced by the proposed direct MPC are shown in Fig. 6. As can be seen, even though the harmonic energy for both $\boldsymbol{i}_{g,abc}$ and $\boldsymbol{v}_{\text{pcc},abc}$ is spread over a wide range of frequencies due to the variable switching frequency, the grid codes, such as the IEEE 519 and IEC 61000-2-4 standards, are met with $I_{g,\text{TDD}} \approx 1.25\%$ and $V_{\text{pcc,TDD}} \approx 3.03\%$. For comparison purposes the spectra of conventional space vector modulation (SVM) are shown in the same figure, while considering the same f_{sw}. This is like having a simple closed-loop linear controller with a very low bandwidth [16]. As can be seen, the TDD values of both current and PCC voltage produced by SVM are higher than those obtained with MPC.

Conclusions

This paper presented a long-horizon direct MPC algorithm for an MV 3L-NPC converter connected to the grid via an LCL filter. The control problem formulation is augmented with output constraints that relate to physical limitations of the system components. The underlying optimization problem is formulated as an ILS problem where the output constraints are translated into input constraints that define a new feasible set. Subsequently, the employed sphere decoder finds the feasible point within the refined hypersphere in a computationally efficient manner. In doing so, operation within the safety operating region of the system is guaranteed without deteriorating its performance. As shown, the proposed approach

[6] Note that the constraint $\|\Delta\boldsymbol{u}(\ell)\|_\infty \leq 1$ is activated and fully respected in both MPC formulations.

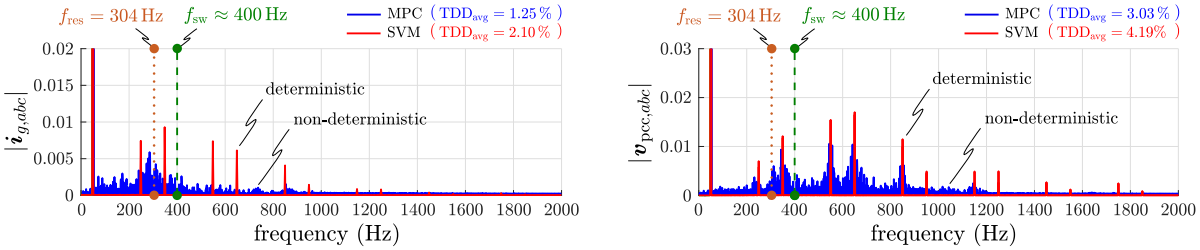

Fig. 6: Harmonic spectra of (a) $\boldsymbol{i}_{g,abc}$, and (b) $\boldsymbol{v}_{\text{pcc},abc}$ in p.u. For both cases, the harmonics do not violate their respective limits (in terms of TDD and amplitude) imposed by the IEEE 519 and IEC 61000-2-4 standards.

achieves excellent steady-state and transient performance, while meeting the relevant grid codes despite the low switching frequency which is very close to the resonance one. Finally, thanks to the adopted long prediction horizon and the full-state information, an additional active damping loop is unnecessary, resulting in a simpler control architecture compared to conventional control strategies.

References

[1] IEEE Std 519-2014 (Revision of IEEE Std 519-1992), "IEEE recommended practices and requirements for harmonic control in electrical power systems," pp. 1–29, Jun. 2014.

[2] IEC 61000-2-4, "Electromagnetic compatibility (EMC)—part 2-4: Environment—compatibility levels in industrial plants for low-frequency conducted disturbances," Sep. 2002.

[3] J. Dannehl, F. W. Fuchs, S. Hansen, and P. B. Thøgersen, "Investigation of active damping approaches for PI-based current control of grid-connected pulse width modulation converters with LCL filters," *IEEE Trans. Ind. Appl.*, vol. 46, no. 4, pp. 1509–1517, Jul./Aug. 2010.

[4] P. C. Loh and D. Holmes, "Analysis of multiloop control strategies for $LC/CL/LCL$-filtered voltage-source and current-source inverters," *IEEE Trans. Ind. Appl.*, vol. 41, no. 2, pp. 644–654, Mar./Apr. 2005.

[5] T. Geyer, *Model predictive control of high power converters and industrial drives*. Hoboken, NJ, USA: Wiley, 2016.

[6] P. Karamanakos, E. Liegmann, T. Geyer, and R. Kennel, "Model predictive control of power electronic systems: Methods, results, and challenges," *IEEE Open J. Ind. Appl.*, vol. 1, pp. 95–114, 2020.

[7] P. Cortés, M. P. Kazmierkowski, R. M. Kennel, D. E. Quevedo, and J. Rodriguez, "Predictive control in power electronics and drives," *IEEE Trans. Ind. Electron.*, vol. 55, no. 12, pp. 4312–4324, Dec. 2008.

[8] T. Geyer and D. E. Quevedo, "Multistep finite control set model predictive control for power electronics," *IEEE Trans. Power Electron.*, vol. 29, no. 12, pp. 6836–6846, Dec. 2014.

[9] P. Karamanakos., T. Geyer, and R. Kennel, "Constrained long-horizon direct model predictive control for power electronics," in *Proc. IEEE Energy Convers. Congr. Expo.*, Milwaukee, WI, USA, Sep. 2016, pp. 1–8.

[10] M. Rossi, P. Karamanakos, and F. Castelli-Dezza, "An indirect model predictive control method for grid-connected three-level neutral point clamped converters with LCL filters," *IEEE Trans. Ind. Appl.*, vol. 58, no. 3, pp. 3750–3768, May/Jun. 2022.

[11] P. Karamanakos and T. Geyer, "Guidelines for the design of finite control set model predictive controllers," *IEEE Trans. Power Electron.*, vol. 35, no. 7, pp. 7434–7450, Jul. 2020.

[12] P. Karamanakos, T. Geyer, and R. Kennel, "Reformulation of the long-horizon direct model predictive control problem to reduce the computational effort," in *Proc. IEEE Energy Convers. Congr. Expo.*, Pittsburgh, PA, USA, Sep. 2014, pp. 3512–3519.

[13] J. B. Rawlings and D. Q. Mayne, *Model predictive control: Theory and design*. Madison, WI: Nob Hill, 2009.

[14] P. Karamanakos and T. Geyer and R. Kennel, "Suboptimal search strategies with bounded computational complexity to solve long-horizon direct model predictive control problems," in *Proc. IEEE Energy Convers. Congr. Expo.*, Montreal, QC, Canada, Sep. 2015, pp. 334–341.

[15] T. Geyer, P. Karamanakos, and R. Kennel, "On the benefit of long-horizon direct model predictive control for drives with LC filters," in *Proc. IEEE Energy Convers. Congr. Expo.*, Pittsburgh, PA, USA, Sep. 2014, pp. 3520–3527.

[16] M. Rossi, E. Liegmann, P. Karamanakos, F. Castelli-Dezza, and R. Kennel, "Long-horizon direct model predictive control for a series-connected modular rectifier," in *Proc. Int. Exhib. and Conf. for Power Electron., Intell. Motion, Renew. Energy and Energy Manag.*, Nuremberg, Germany, 2020, pp. 342–349.